Temporal and Spatial Variations of Global Deep Cloud Systems Based on CloudSat and CALIPSO Satellite Observations

PENG Jie[1,2], ZHANG Hua[*3], and Zhanqing LI[1,4]

[1]*College of Global Change and Earth System Science, Beijing Normal University, Beijing* 100875
[2]*Shanghai Meteorological Bureau, Shanghai* 200030
[3]*Laboratory for Climate Studies, China Meteorological Administration, National Climate Center, Beijing* 100081
[4]*Department of Atmospheric and Oceanic Sciences & Earth System Science Interdisciplinary Center,*
University of Maryland, College Park, MD 20740, *USA*

ABSTRACT

The spatial and temporal global distribution of deep clouds was analyzed using a four-year dataset (2007–10) based on observations from CloudSat and CALIPSO. Results showed that in the Northern Hemisphere, the number of deep cloud systems (DCS) reached a maximum in summer and a minimum in winter. Seasonal variations in the number of DCS varied zonally in the Southern Hemisphere. DCS occurred most frequently over central Africa, the northern parts of South America and Australia, and Tibet. The mean cloud-top height of deep cloud cores (TDCC) decreased toward high latitudes in all seasons. DCS with the highest TDCC and deepest cores occurred over east and south Asian monsoon regions, west-central Africa and northern South America. The width of DCS (WDCS) increased toward high latitudes in all seasons. In general, DCS were more developed in the horizontal than in the vertical direction over high latitudes and vice versa over lower latitudes. Findings from this study show that different mechanisms are behind the development of DCS at different latitudes. Most DCS at low latitudes are deep convective clouds which are highly developed in the vertical direction but cover a relatively small area in the horizontal direction; these DCS have the highest TDCC and smallest WDCS. The DCS at midlatitudes are more likely to be caused by cyclones, so they have less vertical development than DCS at low latitudes. DCS at high latitudes are mainly generated by large frontal systems, so they have the largest WDCS and the smallest TDCC.

Key words: deep cloud, deep cloud core, aerosol invigoration effect

Citation: Peng, J., H. Zhang, and Z. Q. Li, 2014: Temporal and spatial variations of global deep cloud systems based on CloudSat and CALIPSO satellite observations. *Adv. Atmos. Sci.*, **31**(3), 593–603, doi: 10.1007/s00376-013-3055-6.

1. Introduction

Clouds and their interactions with atmospheric circulation, shortwave and longwave radiation, and the surface are very important components of both weather and climate. Serving as one of the most important elements of hydrological and energy circulation, clouds have a crucial impact not only on radiation budgets at the surface and the top-of-the-atmosphere, but also on heating profiles within the atmosphere and the spatial and temporal distribution of precipitation around the globe. Usually accompanied by precipitation, deep cloud systems (DCS) have a more direct impact on hydrologic circulation, and absorb much more surface longwave radiation and reflect more shortwave solar radiation than do shallow clouds. Satellite-based studies (Ramanathan et al., 1989; Harrison et al., 1990; Hartmann et al., 1992;

Kiehl, 1994; Hartmann et al., 2001; Futyan and Del Genio, 2007) have revealed that the mean net radiative forcing of DCS over large spatial scales and over long time periods is close to zero because of the cancellation of strong negative shortwave forcing and strong positive longwave forcing. Yuan and Li (2010) and Yuan et al. (2010) used moderate resolution imaging spectroradiometer (MODIS) data to study macro- and micro-physical properties of deep convective clouds. They found that the optical depth of deep convective clouds varies slightly over the course of a year and that the particle size of ice crystals at the top of deep convective clouds are positively correlated to the brightness temperature, although the correlation varied over time and space. They also developed a method to estimate glaciation temperatures inside deep convective clouds. Using a combination of CloudSat and atmospheric infrared sounder data, as well as output from the Global Data Assimilation System model, Savtchenko (2009) found that deep convective clouds humidified the upper level of the troposphere and reduced the

---

* Corresponding author: ZHANG Hua
  Email: huazhang@cma.gov.cn

amount of outgoing longwave radiation under all-sky conditions. Sassen et al. (2009) explored the correlation between deep convective clouds and cirrus clouds over tropical regions. Using data from the A-train constellation of satellites, Iwasaki et al. (2010) estimated the mean radius of ice crystals and the mean ice water content above a level with a potential temperature of 380 K (near the top of the troposphere) in deep convective clouds to be 23.0 ± 4.9 μm and 7.2 ± 8 mg m^{-3}, respectively. Yuan and Houze (2010) and Yuan et al. (2011) analyzed the 3D structure of deep convective cloud anvils on a global scale, based on MODIS/Advanced Microwave Scanning radiometer observations. Takahashi and Luo (2012) analyzed the level of neutral buoyancy for deep convective clouds based on CloudSat data. While interactions between clouds, aerosols, radiation and precipitation contribute toward one of the largest uncertainties in the field of climate change, recent studies (Rosenfeld et al., 2008; Li et al., 2011) suggest that aerosols could also influence the development of DCS.

Aerosols can serve as cloud condensation nuclei, so they can modify cloud radiative and dynamical properties. The effect of aerosols on cloud life time and precipitation is often referred to as the "aerosol indirect effect". Studies (Albrecht, 1989; Radke et al., 1989; Rosenfeld, 2000; Ramanathan et al., 2001; Andreae et al., 2004; Li et al., 2011) have suggested that, with a fixed amount of water, an influx of aerosols could lead to the formation of more but smaller cloud droplets, thus suppressing collision and coalescence processes. The number of cloud droplets that could grow large enough to start rainfall would then be reduced, resulting in less precipitation. When deep mixed-phase clouds are formed under suitable dynamical conditions, more aerosols could enhance the development of these clouds in the following way. In the presence of a high concentration of aerosols, smaller cloud droplets could weaken, or even completely shut down, downdrafts within the cloud. Updrafts could then move these cloud droplets higher into the cloud. Once they pass the freezing level and start condensing, more latent heat would be released which would allow the cloud to grow more vigorously. This mechanism is the so-called aerosol invigoration effect (AIE) (Rosenfeld et al., 2008). Although both modeling and observational studies (Khain et al., 2005; Koren et al., 2005; Tao et al., 2007; Lee et al., 2010; Li et al., 2011; Freud and Rosenfeld, 2012; Niu and Li, 2012) have reported evidence to support the AIE and pointed out that it is particularly important for mixed-phase deep clouds, more work is still needed to further understand the AIE and its possible impact on climate and extreme weather. As modeling studies have shown (Khain et al., 2005; Tao et al., 2007), the AIE is more significant under certain conditions, such as with sufficient water vapor supply and weaker wind shear, but it is much weaker under opposite conditions, and such conditions are different for mixed-phase deep clouds at different geo-locations/time periods. Thus, better understanding of the temporal and spatial distribution of global DCS will help to reveal the best time and location to study the AIE. Therefore, in the present reported study, the global distribution of DCS was analyzed using four years' worth of CloudSat/Cloud-Aerosol Lidar and Infrared Pathfinder Satellite Observation(CALIPSO) data in order to build the foundation for a future, more in-depth study on the large-scale AIE. Section 2 describes the algorithm developed to identify DCS. The global frequency of DCS and the global distribution of the macro-physical properties of DCS are presented in sections 3 and 4, respectively. Conclusions and a discussion are given in section 5.

2. Algorithm for identifying DCS

2.1. *CloudSat data*

CloudSat is a polar-orbiting satellite and is a member of National Aeronautics and Space Administration (NASA)'s A-train constellation, launched in April 2006. The satellite carries a 94-GHz nadir-view cloud profiling radar (CPR) that can objectively observe clouds at a high vertical resolution. It is in a sun-synchronous orbit at an altitude of 705 km with an orbit period of about 98.9 minutes during which time approximately 37 081 profiles are generated. The resolution for each pixel in the horizontal direction is 1.1 km along the orbit swath tracking and 1.4 km perpendicular to the orbit tracking and 0.24 km in the vertical direction. With the combination of observations from CloudSat and CALIPSO, as well as reanalysis data from the European Centre for Medium-Range Weather Forecasts (ECMWF), CloudSat standard products provide the macro/micro-physical and radiative properties of cloud as well as the meteorological parameters in each pixel.

In our studies, 2B-GEOPROF and 2B-GEOPROF-LIDAR were used to determine the location of DCS. Both products provide the cloud geometry information but measured from different instruments. 2B-GEOPROF provides the radar echo in each pixel from the CPR, which has strong penetrability and can therefore detect low-level cloud with thick cloud above. 2B-GEOPROF-LIDAR contains information from the Cloud-Aerosol Lidar with Orthogonal Polarization (CALIOP) aboard CALIPSO, which can observe very thin ice cloud that the CPR cannot. Therefore, a combination of both products has the benefit of both radar and lidar data and thus provides more accurate cloud detections.

Using cloud mask, cloud fraction and radar reflectivity data from the 2B-GEOPROF and 2B-GEOPROF-Lidar products, pixels were identified as clear or cloudy. The cloud mask indicates that each pixel is detected by the CPR and that the threshold for cloud existing is larger than 20. The cloud fraction contains the percentage within each pixel that is identified by the lidar as cloud. The radar reflectivity is the radar echo from the CPR within each pixel. Since the minimum detectable signal of the CPR is approximately -30 dBZ, if the pixel has a cloud mask flag < 20 and a cloud fraction $\geqslant 50\%$ or a reflectivity $\geqslant -30$ dBZ and a cloud mask flag $\geqslant 20$, the pixel is cloudy; in all other cases the pixel is clear (Zhang et al., 2013; Peng et al., 2013).

2.2. *Identifying DCS*

No universal definition of DCS has been established even though related studies about DCS have been published by

others. In this study, which focuses on how deep mixed-phase clouds might be affected by the AIE, cloud top and base heights were used to define DCS. CloudSat records cloud information continuously along its orbital track, so it provides not only single profile information but also information on the cross-section formed by the combination of adjacent profiles. Following the method used in Luo et al. (2010), we first identified a cloudy profile which was strongly developed in the vertical direction and defined it as a deep cloud core (DCC); the DCC and adjacent cloudy pixels in the cross-section were then defined as DCS. The AIE is most significant in deep mixed-phase clouds with cloud bases lower than 2 km (Li et al., 2011), so only those DCC that are single-layered with a cloud-top height > 10 km and with a distance < 2 km between the surface and the cloud base were considered. Once a DCC was identified, adjacent profiles in both forward and backward directions along track were examined and if there were cloudy pixels at the same altitude in connected profiles, they were deemed associated with the same deep cloud. This process continued in expanding directions until no cloudy pixels in connecting profiles were found; at this point, a DCS had been identified.

An example of a DCS is shown in Fig. 1, taken from CloudSat orbit 4108 on 4 February 2007. This DCS includes 214 DCC and covers a horizontal range of 1841.1 km.

Studies (Huang et al., 2005, 2006) have demonstrated the importance of multi-layer clouds to the radiation budget and have developed algorithms for the identification of multi-layer clouds and the retrieval of their properties. So if any deep cloud is overlapped by other cloud, such as cirrus, it is not considered as a DCC, which leads to an underestimate of the number of global DCS. All data were checked to estimate the uncertainties. If the lowest-layer cloud of any multi-layer cloudy profile had a cloud-top height > 10 km and a distance < 2 km between the surface and the cloud base, the multi-layer profile was considered to be a miss-identified DCC. According to the geographical location and UTC time of the misidentified DCC, we found that most of them were included in the currently identified DCS. Then, we checked all misidentified DCC that were not included in the current DCS, and if the number of continuously misidentified DCC not included in the current DCS was larger than five, they were considered to be missed-DCS. So, the ratio of the number of missed-DCS to the number of DCS was considered to be the underestimate of global DCS, which ranged from about 5% in low latitudes to about 2% in high latitudes.

3. Global distribution and seasonal trends in DCS

The global distribution of DCS and seasonal trends in the number of DCS (NDCS) are examined in this section. First, the Southern and Northern Hemispheres (SH and NH, respectively) were each divided into zones: low latitude (LL: 0°–30°), midlatitude (ML: 30°–60°) and high latitude (HL: 60°–90°). Seasons were defined as follows:

(1) December, January and February for winter in the NH and summer in the SH;

(2) March, April and May for spring in the NH and autumn in the SH;

(3) June, July and August for summer in the NH and winter in the SH;

(4) September, October and November for autumn in the
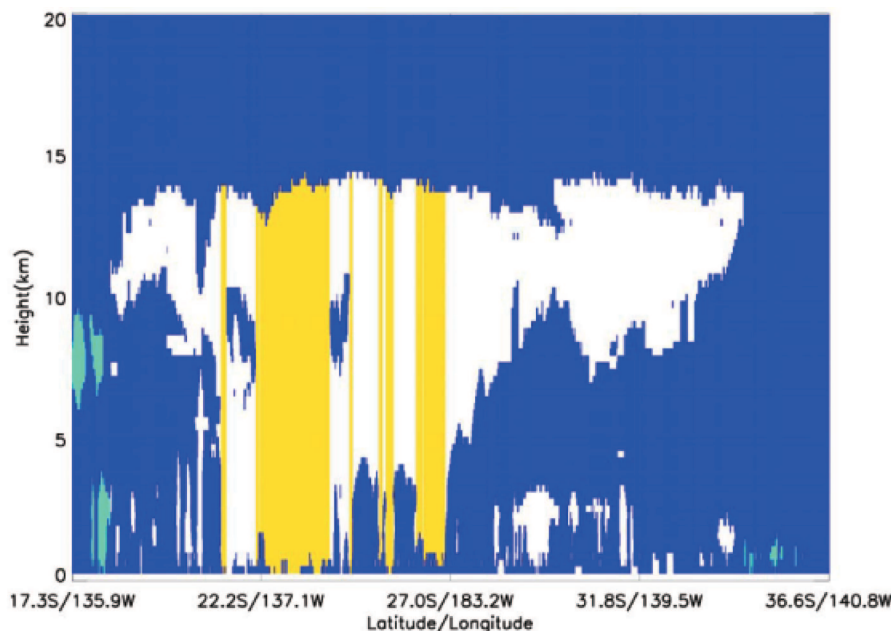
Fig. 1. Example of a DCS identified on 4 Feb 2007. White and yellow areas represent the DCS (the yellow area is the DCC) and blue regions are clear sky; green areas represent cloudy pixels not classified as part of the DCS.

NH and spring in the SH.

The mean latitude and longitude of all the DCC in each DCS was used to represent the location of the DCS; they were calculated over $5° \times 5°$ grid boxes. The NDCS was calculated as the sum of the DCS in each grid box per season over the four-year period. Figure 2 shows the monthly time series of NDCS in different zonal bands. In the NH, the NDCS changes significantly with season in all zonal bands; the maximum NDCS occurs in summer and the minimum in winter (Fig. 2a). In the LL zone of the SH, the maximum NDCS also occurs in summer and the minimum in winter; in the HL zone in the SH, the reverse is seen (Fig. 2b). The NDCS remains generally the same year-round in the ML zone of the SH. Globally, for any single month over the four-year period,

the maximum NDCS (4221) occurred in August 2007 and the minimum NDCS (561) occurred in April 2010.

Convective instability caused by radiative heating is the main contributing factor toward the generation of DCS in the LL zone of both hemispheres, which explains why the NDCS in this zonal band is large in summer and small in winter. Figures 2c–f demonstrate how different underlying surfaces can lead to large differences in the seasonal variation of the NDCS in the ML and HL zones of both hemispheres. The seasonal variations of the NDCS over land and over the ocean in the LL zone are the same. The much larger NDCS over the ocean than over land is because many tropical cyclones are generated over the ocean in the LL zone. The seasonal variation of the NDCS over land in the NH (Fig. 2c, dash–
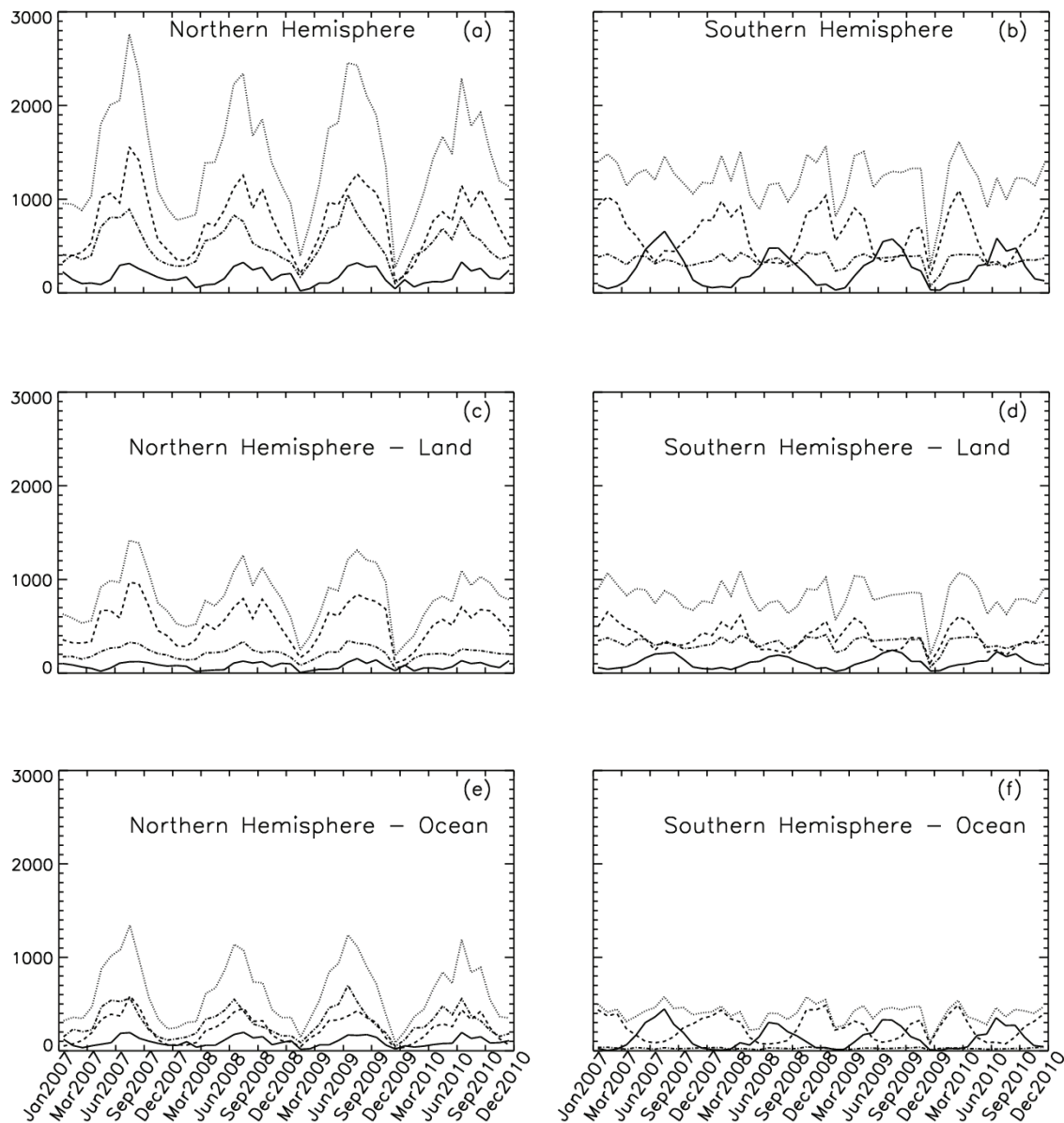
Fig. 2. Total NDCS per month in different zonal bands for (a) the NH, (b) the SH, (c) the NH over land, (d) the SH over land, (e) the NH over the ocean, and (f) the SH over the ocean. The dotted line represents the NDCS over all zonal bands; the dashed line is for $0°–30°$; the dash–dot line is for $30°–60°$; and the solid line is for $60°–90°$.

dot line) is much more significant than over the oceans (Fig. 2e, dash–dot line) because cloud development over land is more complex. Oceans dominate in the ML zone of the SH so cloud formation is a simpler process over this surface and little seasonal variation is seen in the NDCS (Fig. 2f). The largest NDCS in the HL zone occurs in the SH where the sub-polar low is located. DCS here are formed from the convergence of cold air from the polar region and warm air from the subtropical region.

The NDCS for different zonal regions and seasons is summarized in Table 1; the global distribution of NDCS for each season is shown in Fig. 3. The global distribution of NDCS are consistent with previous deep-cloud-related studies (Sassen et al., 2009; Savtchenko, 2009), which indicate that the representation according to CloudSat/CALIPSO's observations is still reasonable despite the limited spatial and temporal resolution. The maximum NDCS (39 343) occurs

in the NH summer/SH winter and the minimum NDCS (23 827) occurs in the NH winter/SH summer. The highest density of DCS occurs in central Africa, northern South America, Indonesia and Tibet, with the maximum values of NDCS in a single grid box within each of these regions over the four-year period being 86, 112, 87 and 154, respectively. Note the significant increase in the NDCS over the Antarctic polar region during NH summer/SH winter (Fig. 3b).

4. Macrophysical properties of DCS on a global scale

AIE-related studies have reported that deep mixed-phase clouds tend to have higher cloud-top heights and lower cloud-top temperatures under polluted conditions than under clean conditions (Li et al., 2011; Niu and Li, 2012). Using a

Table 1. Total number of DCS in different zonal regions for different seasons over the period 2007–10.

	LL/NH	ML/NH	HL/NH	Total/NH	LL/SH	ML/SH	HL/SH	Total/SH
Spring NH/Autumn SH	7971	6063	1107	15 141	9414	4454	1917	15 785
Summer NH/Winter SH	13 006	9367	2968	25 341	4222	4076	5705	14 003
Autumn NH/Spring SH	11 524	5954	2543	20 021	6759	4145	3709	14 613
Winter NH/Summer SH	4296	3563	1711	9570	9479	3977	801	14 257
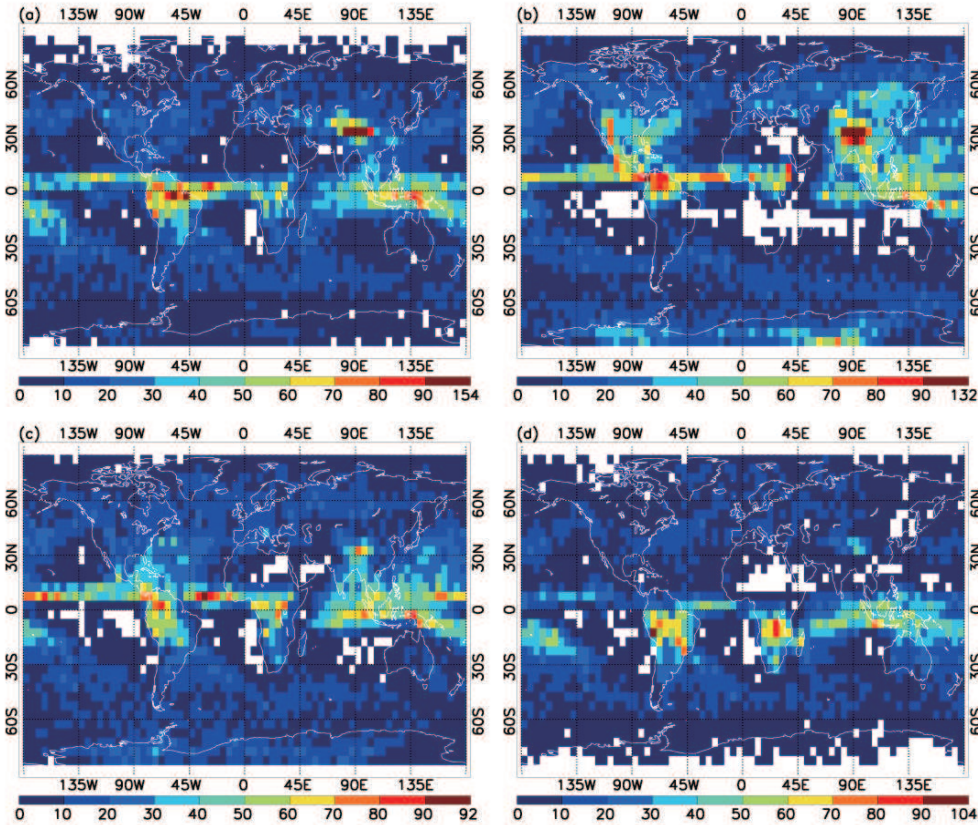
Fig. 3. Total number of DCS in each $5° \times 5°$ grid box over the four-year period for (a) NH spring/SH autumn, (b) NH summer/SH winter, (c) NH autumn/SH spring, and (d) NH winter/SH summer. White grid boxes signify that no DCS were identified in that box.

combination of MODIS retrievals and Goddard Chemistry Aerosol Radiation and Transport model simulations, Khain et al. (2005) found that when the aerosol optical depth increases, the ratio of clouds with large optical depths to those with small optical depths decreases. They explained that with an increase in aerosol loading, the most vertically developed part of a DCS (high optical depth) would intensify, and the horizontal extent of the anvil (small optical depth) would increase. These findings suggest that both the vertical and horizontal macrophysical properties of a DCS can be modified through the AIE. The mean distance between the top of each DCC and the surface within a single DCS (cloud-top height of deep cloud cores; TDCC) and the mean depth of the deep cloud core (DDCC) are used to describe the strength of the vertical development. The horizontal development of a DCS is expressed as the cross-sectional width of the DCS (WDCS).

4.1. *Global distribution and seasonal trends in TDCC*

Figure 4 shows the monthly time series of the mean TDCC over the four-year period. There is little seasonal variation in the mean TDCC in the LL and HL zones of the NH. The mean TDCC in the ML zone of the NH reaches a maximum in summer (10.59 km) and a minimum in winter (9.89 km). In the SH, the highest TDCC occurs in the LL and ML zones in summer (13.51 km and 11.03 km, respectively) and the lowest TDCC occurs in these regions in winter (13.00 km and 10.77 km). The mean TDCC in the HL zone of the SH varies greatly from month-to-month (Fig. 4b) but there is little difference in TDCC between different seasons (Table 2). Global distributions of TDCC and DDCC for different seasons are shown in Figs. 5 and 6, respectively. The TDCC decreases toward higher latitudes in both hemispheres; the mean TDCCs from the HL to the LL zone are 9.97 km, 10.47 km and 13.24 km. The lowest TDCC and smallest DDCC can be seen over Tibet, Greenland, the Antarctic continent and Chilean plateaus. Because TDCC is defined as the distance between the cloud top and the surface and DCC is defined as a single-layered cloud with top heights greater than 10 km above mean sea level, the DCC over these elevated land surfaces have the lowest TDCC. The DCS with the highest TDCC (up to 16 km) and largest DDCC ($\sim$ 15 km) occur over south and eastern Asian monsoon regions, west-central Africa and northern South America. Note that the DCS grows thicker and higher in the winter over the Antarctic (Figs. 5b and 6b).

4.2. *Global distribution and seasonal trends in WDCS*

Figure 7 shows the monthly time series of the mean WDCS over the four-year period; Table 3 summarizes the mean WDCS for different zonal regions and seasons. The maximum and minimum WDCS in the NH are 1055.9 km (in winter) and 645.2 km (in summer), respectively. Large-scale circulation in winter is mainly in the form of frontal systems, which are much larger in scale than summertime convective cloud systems, so although fewer DCS are seen in the NH during winter (Table 1), they are much larger in horizontal extent. In the SH, the maximum WDCS occurs in the HL zone in the autumn (1364.7 km) and the minimum WDCS can be seen in the LL zone in the winter (585.7 km).

The global distribution of WDCS is shown in Fig. 8. The main feature that can be seen is the increase in WDCS to-
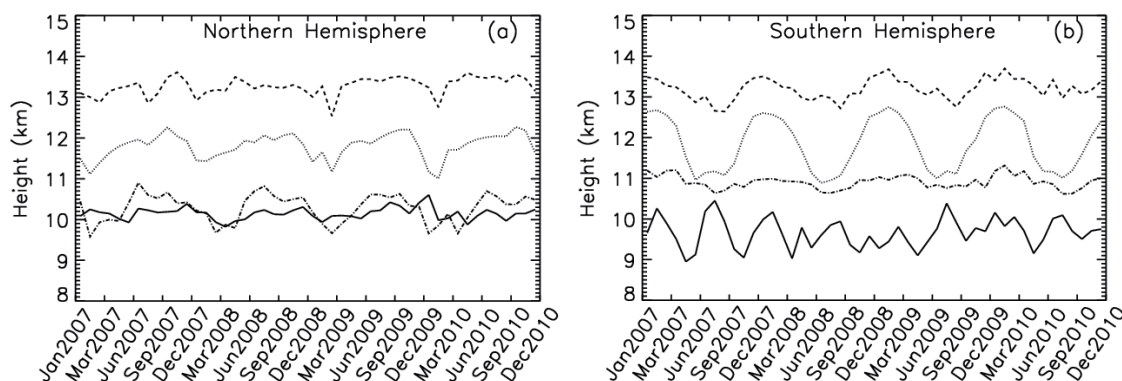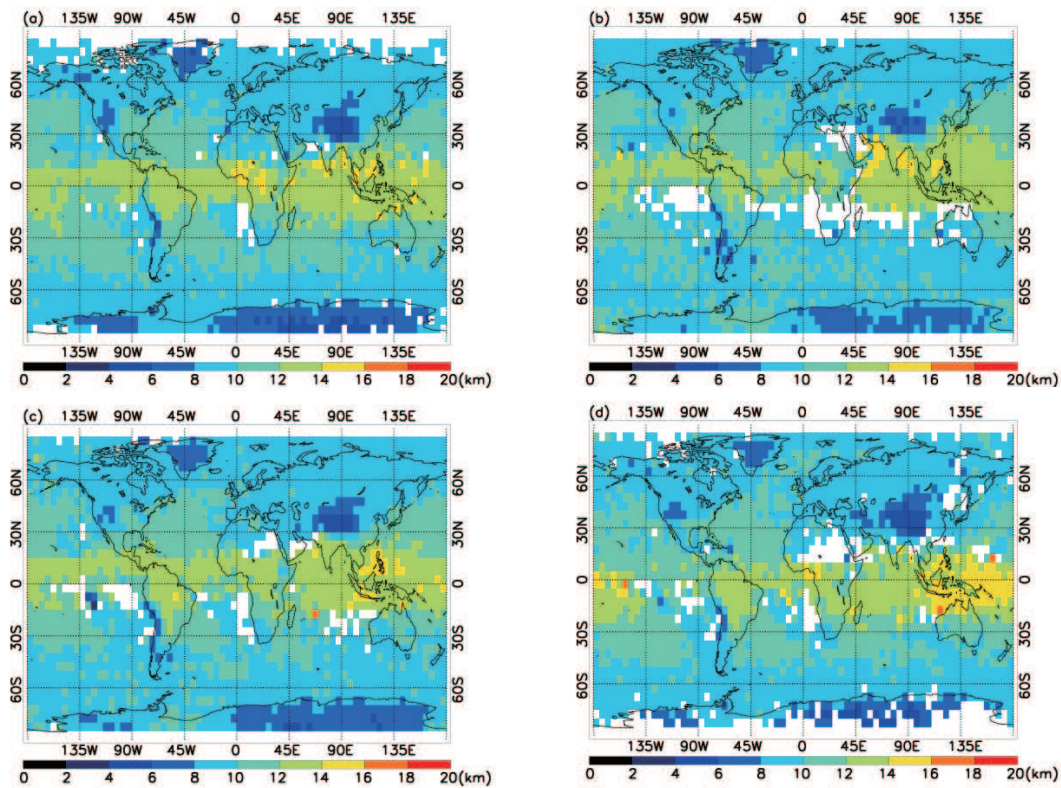

Fig. 4. Monthly time series of mean TDCC over the four-year period for different zonal bands in (a) the NH and (b) the SH. The dotted line represents TDCC over all zonal bands; the dashed line is for 0°–30°; the dash–dot line is for 30°–60°; and the solid line is for 60°–90°.

Table 2. Mean TDCC in different zonal regions for different seasons over the period 2007–10 (units: km).

|	LL/NH	ML/NH	HL/NH	Total/NH	LL/SH	ML/SH	HL/SH	Total/SH
Spring NH/Autumn SH	13.22	10.14	10.04	11.64	13.26	11.02	9.50	12.15
Summer NH/Winter SH	13.34	10.59	10.15	11.95	13.00	10.77	9.81	11.08
Autumn NH/Spring SH	13.40	10.49	10.18	12.12	13.03	10.81	9.57	11.55
Winter NH/Summer SH	13.12	9.89	10.22	11.49	13.51	11.03	9.79	12.60
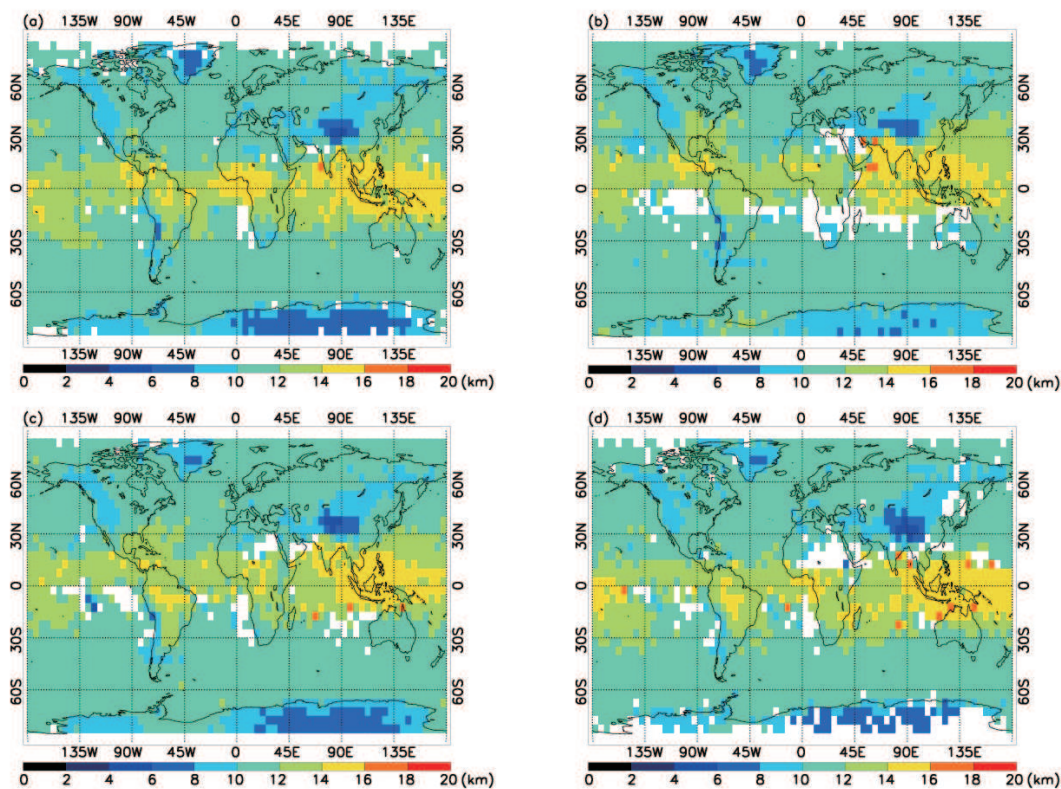
Fig. 5. Mean TDCC in each $5° \times 5°$ grid box over the four-year period for (a) NH spring/SH autumn, (b) NH summer/SH winter, (c) NH autumn/SH spring, and (d) NH winter/SH summer. White grid boxes signify that no DCS were identified in that box.
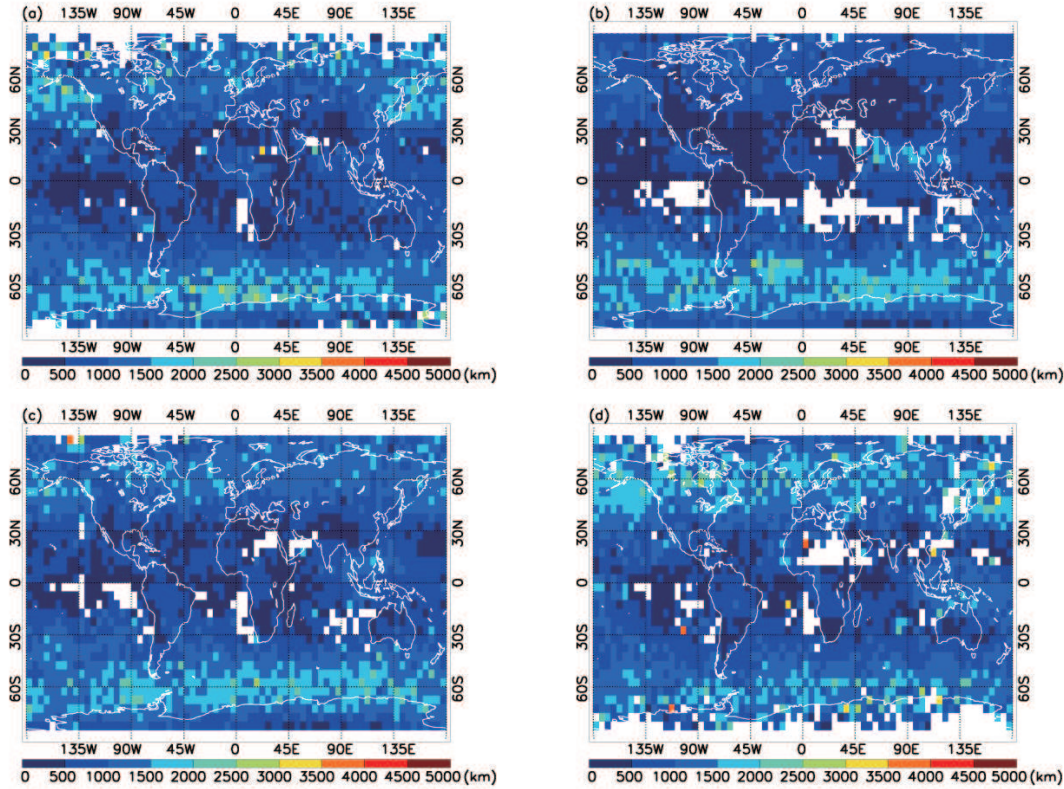

Fig. 6. Same as Fig. 5 but for mean DDCC.
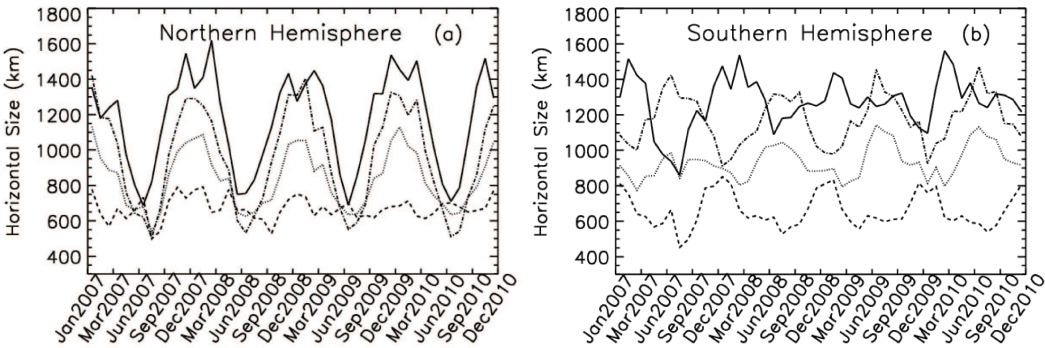
Fig. 7. Monthly time series of mean WDCS over the four-year period for different zonal bands in (a) the NH and (b) the SH. The dotted line represents WDCS over all zonal bands; the dashed line is for 0°–30°; the dash–dot line is for 30°–60°; and the solid line is for 60°–90°.

Fig. 8. Mean WDCC in each 5°×5° grid box over the four-year period for (a) NH spring/SH autumn, (b) NH summer/SH winter, (c) NH autumn/SH spring, and (d) NH winter/SH summer. White grid boxes signify that no DCS were identified in that box.

Table 3. Mean WDCS in different zonal regions for different seasons over the period 2007–10 (units: km).

	LL/NH	ML/NH	HL/NH	Total/NH	LL/SH	ML/SH	HL/SH	Total/SH
Spring NH/Autumn SH	647.2	1017.4	1263.8	844.1	618.5	1115.4	1364.7	846.4
Summer NH/Winter SH	657.9	588.8	779.7	645.2	585.7	1337.5	1168.8	1036.8
Autumn NH/Spring SH	643.6	925.9	1232.2	801.0	633.9	1230.4	1245.1	964.2
Winter NH/Summer SH	730.8	1295.0	1383.1	1055.9	802.8	1021.1	1313.4	890.5

ward higher altitudes; the mean WDCS in the LL, ML and HL zones in both hemispheres is 665.05 km, 1066.44 km and 1218.85 km, respectively. Over the four-year period, the DCS with the largest WDCS are seen in the HL zone of the SH; this is attributed to the presence of the sub-polar low and the resulting generation of large-scale DCS. Worth to note that, when we calculate the WDCS for any particularly grid, the profile not in the grid may also be taken into the consideration as long as it belongs to the DCS that the averaged latitude and longitude of its DCCs lies in the grid. Therefore, although the length of each grid is different in different latitudes, it will not influence the result of WDCS.

4.3. *Reasons behind the distribution of macrophysical properties of DCS*

Seasonal variations of TDCC and DDCC in different zonal regions are mainly due to the different mechanisms for generating DCS at different latitudes. Using reanalysis data from the ECMWF, convective available potential energy (CAPE) was calculated; this quantity is often used to represent convective intensity. Figure 9 shows the monthly time series of mean CAPE over the four-year period for different zonal bands. In general, the TDCC is positively correlated to CAPE at different latitudes. The DCS in the LL zone are mainly deep convective clouds, highly developed in the vertical direction but covering a relatively small area in the horizontal direction. The generation of clouds in the ML zone is highly impacted by mesoscale weather systems, so many DCS are formed along fronts; strong monsoons also influence the generation of DCS. In the ML zone of the NH, the significant increase in the number of deep cumulonimbi during the summer results in an increase in TDCC. In the SH, oceans are the dominant surface in the ML zone, so there is much less variation in conditions producing DCS throughout the year. Convection is weakest in the HL zone in both hemispheres, so DCS are mainly generated by large-scale frontal

Fig. 9. Monthly time series of mean CAPE over the four-year period for different zonal bands.

systems; TDCC (WDCS) decreases (increases) toward higher latitudes.

5.   Discussion and conclusions

Using four years' worth of CloudSat and CALIPSO data (2007–10), DCS were identified and the global distribution of the number of DCS, TDCC, DDCC and WDCS was analyzed. The main conclusions are as follows:

(1) The greatest concentration of DCS occurred in central Africa, northern South America, northern Australia and Tibet; the maximum values of NDCS in a single grid box within each of these regions over the four-year period were 86, 112, 87 and 154, respectively. There was a significant increase in the NDCS over the Antarctic polar region during NH summer/SH winter. In the NH, the fewest NDCS were seen in winter (9570) and the greatest NDCS occurred in summer (25 341); the total number of DCS in spring and autumn were 15 141 and 20 021. There was more seasonal and zonal variation in NDCS in the SH. The maximum NDCS seen in the LL zone occurred in summer (9479) and the minimum in winter (4222); in the HL zone in the SH, the reverse was seen (winter: 5705, summer: 801). The NDCS remained generally the same year-round in the ML zone of the SH.

(2) TDCC decreased toward higher latitudes in both hemispheres. The DCS with the highest TDCC (up to 16 km) and largest DDCC ($\sim$ 15 km) occurred over south and eastern Asian monsoon regions, west-central Africa and northern South America. There was little seasonal variation in the mean TDCC in the LL and HL zones of the NH. The mean TDCC in the ML zone of the NH reached a maximum in summer (10.59 km) and a minimum in winter (9.89 km). In the SH, the highest TDCC occurred in the LL and ML zones in summer (13.51 km and 11.03 km, respectively) and the lowest TDCC occurred in these regions in winter (13.00 km and 10.77 km). The mean TDCC in the HL zone of the SH varied greatly from month-to-month but there was little difference in TDCC between different seasons.

(3) The WDCS increased in magnitude toward higher latitudes; the mean WDCS in the LL, ML and HL zones of both hemispheres was 665.05 km, 1066.44 km and 1218.85 km, respectively. Over the four-year period, the DCS with the largest WDCS were found in the HL zone of the SH. The maximum and minimum WDCS in the NH was 1383.1 km (winter) and 645.2 km (summer), respectively. The WDCS in the LL zone of the SH was largest in summer (802.8 km) and smallest in winter (585.7 km). In the ML zone of the SH, the maximum (minimum) WDCS (1337.5 km; 1021.1 km) occurred in winter (summer). The largest and smallest WDCS were seen in autumn and winter in the HL zone of the SH (1364.7 km and 1168.8 km, respectively).

(4) Seasonal variations of TDCC and DDCC in different zonal regions are mainly due to the different mechanisms for generating DCS at different latitudes. The DCS in the LL zone are mainly deep convective clouds, highly developed in the vertical direction but covering a relatively small area
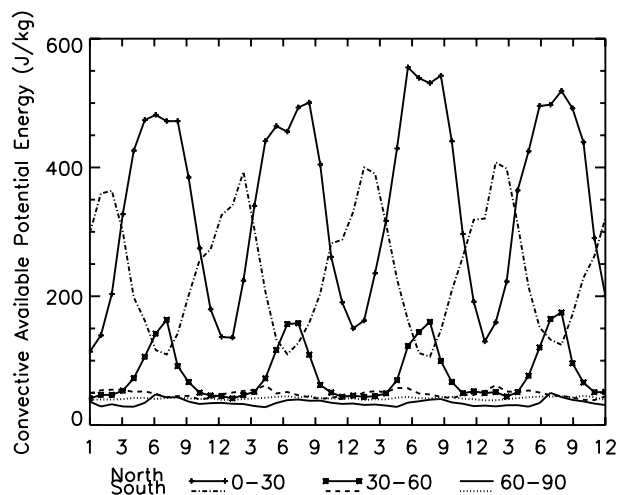
in the horizontal direction. Most DCS in the ML zone are formed by frontal systems, so they have smaller TDCC than those in the LL zone. The NDCS in the ML zone of the NH (SH) increases significantly in summer (winter) because of the monsoon circulation. The DCS in the HL zone are mainly generated by large frontal systems, so have the largest WDCS and smallest TDCC.

Future work will focus on examining the AIE in DCS at a global scale.

REFERENCES

Albrecht, B. A., 1989: Aerosols, cloud microphysics, and fractional cloudiness. *Science*, **245**, 1227–1230.

Andreae, M. O., D. Rosenfeld, P. Artaxo, A. A. Costa, G. P. Frank, K. M. Longo, and M. A. F. Silva-Dias, 2004: Smoking rain clouds over the Amazon. *Science*, **303**, 1337–1342.

Freud, E., and D. Rosenfeld, 2012: Linear relation between convective cloud drop number concentration and depth for rain initiation. *J. Geophys. Res.*, **117**, D02207, doi: 10.1029/2011JD016457.

Futyan, J. M., and A. D. Del Genio, 2007: Deep convective system evolution over Africa and the tropical Atlantic. *J. Climate*, **20**, 5041–5060.

Harrison, E. F., P. Minnis, B. R. Barkstrom, V. Ramanathan, R. D. Cess, and G. G. Gibson., 1990: Seasonal-variation of cloud radiative forcing derived from the Earth Radiation Budget Experiment. *J. Geophys. Res.*, **95**(D11), 18 687–18 703.

Hartmann, D. L., M. E. Ockert-Bell, and M. L. Michelsen, 1992: The effect of cloud type on earths' energy-balance: Global analysis. *J. Climate*, **5**, 1281–1304.

Hartmann, D. L., L. A. Moy, and Q. Fu, 2001: Tropical convection and the energy balance at the top of the atmosphere. *J. Climate*, **14**, 4495–4511.

Huang, J. P., P. Minnis, B. Lin, Y. H. Yi, M. M. Khaiyer, R. F. Arduini, A. Fan, and G. G. Mace, 2005: Advanced retrievals of multilayered cloud properties using multispectral measurements. *J. Geophys. Res.*, **110**(D15), D15S18, doi: 10.1029/2004JD005101.

Huang, J. P., P. Minnis, B. Lin, Y. H. Yi, T. F. Fan, S. Sun-Mack, and J. K. Ayers, 2006: Determination of ice water path in ice-over-water cloud systems using combined MODIS and AMSR-E measurements. *Geophys. Res. Lett.*, **33**(21), L21801, doi: 10.1029/2006GL027038.

Iwasaki, S., T. Shibata, J. Nakamoto, H. Okamoto, H. Ishimoto, and H. Kubota, 2010: Characteristics of deep convection measured by using the A-train constellation. *J. Geophys. Res.*, **115**, D06207, doi: 10.1029/2009JD013000.

Khain, A., D. Rosenfeld, and A. Pokrovsky, 2005: Aerosol impact on the dynamics and microphysics of deep convective clouds. *Quart. J. Roy. Meteor. Soc.*, **131**, 2639–2663, doi:

10.1256/qj.04.62.

Kiehl, J. T., 1994: On the observed near cancellation between longwave and shortwave cloud forcing in tropical regions. *J. Climate*, **7**, 559–565.

Koren, I., Y. J. Kaufman, D. Rosenfeld, L. A. Remer, and Y. Rudich, 2005: Aerosol invigoration and restructuring of Atlantic convective clouds. *J. Geophys. Res.*, **32**, L14828, doi: 10.1029/2005GL023187.

Lee, S. S., L. Donner, and J. E. Penner, 2010: Thunderstorm and stratocumulus: How does their contrasting morphology affect their interactions with aerosols? *Atmos. Chem. Phys.*, **10**, 6819–6837, doi: 10. 5194/acp-10-6819-2010.

Luo, Y. L., R. H. Zhang, W. M. Qian, Z. Z. Luo, and H. Xin, 2010: Intercomparison of deep convection over the Tibetan Plateau-Asian monsoon region and subtropical North America in boreal summer using CloudSat/CALIPSO data. *J. Climate*, **24**, 2164–2177, doi: 10.1175/2009JCLI4032.1.

Niu, F., and Z. Q. Li, 2012: Systematic variations of cloud top temperature and precipitation rate with aerosols over the global tropics. *Atmos. Chem. Phys.*, **12**, 8491–8498, doi: 10.5194/acp-12-84910-2012.

Li, Z. Q., F. Niu, J. W. Fan, Y. G. Liu, D. Rosenfeld, and Y. N. Ding, 2011: Long-term impacts of aerosols on the vertical development of clouds and precipitation. *Nat. Geosci.*, **4**, 888–894, doi: 10.1038/ngeo1313.

Peng, J., H. Zhang, and X. Y. Shen, 2013: Analysis of vertical structure of clouds in East Asia with CloudSat data. *Chinese J. Atmos. Sci.*, **37**(1), 91–100, doi: 10.3878/j. issn.1006-9895.2012.11188. (in Chinese)

Radke, L. F., J. A. Coakley Jr., and M. D. King, 1989: Direct and remote sensing observations of the effects of ships on clouds. *Science*, **246**, 1146–1149.

Ramanathan, V., R. D. Cess, E. F. Harrison, P. Minnis, B. R. Barkstrom, E. Ahmad, and D. Hartmann, 1989: Cloud-radiative forcing and climate: Results from the Earth Radiation Budget Experiment. *Science*, **243**, 57–63.

Ramanathan, V., P. J. Crutzen, J. T. Kiehl, and D. Rosenfeld, 2001: Aerosols, climate, and the hydrological cycle. *Science*, **294**, 2119–2124.

Rosenfeld, D., 2000: Suppression of rain and snow by urban and industrial air pollution. *Science*, **287**, 1793–1796.

Rosenfeld, D., U. Lohmann, G. B. Rage, C. D. O'Dowd, M. Kulmala, S. Fuzzi, A. Reissell, and M. O. Andreae, 2008: Flood or drought: How do aerosols affect precipitation? *Science*, **321**, 1309–1313.

Sassen, K., Z. E. Wang, and D. Liu, 2009: Cirrus clouds and deep convection in the tropics: Insights from CALIPSO and CloudSat. *J. Geophys. Res.*, **114**, D00H06, doi: 10.1029/2009JD011916.

Savtchenko, A., 2009: Deep convection and upper-tropospheric humidity: A look from the A-Train. *Geophys. Res. Lett.*, **36**, L06814, doi: 10.1029/2009GL037508.

Takahashi, H., and Z. J. Luo, 2012: Where is the level of neutral buoyancy for deepconvection? *Geophys. Res. Lett.*, **39**, L15809, doi: 10.1029/2012GL052638.

Tao, W. K., X. W. Li, A. Khain, T. Matsui, S. Lang, and J. Simpson, 2007: Role of atmospheric aerosol concentration on deep convective precipitation: Cloud-resolving model simulations. *J. Geophys. Res.*, **112**, D24S18, doi: 10.1029/2007JD008728.

Yuan, J., and R. A. Houze Jr., 2010: Global variability of mesoscale convective system anvil structure from A-Train satellite data. *J. Climate*, **23**, 5864–5888, doi:

10.1175/2010JCLI3671. 1.

Yuan, J., R. A. Houze Jr., and A. J. Heymsfield, 2011: Vertical structures of anvil clouds of tropical mesoscale convective systems observed by CloudSat. *J. Atmos. Sci.*, **68**, 1653–1674, doi: 10.1175/2011JAS3687.1.

Yuan, T. L., and Z. Q. Li, 2010: General macro- and microphysical properties of deep convective clouds as observed by MODIS. *J. Climate*, **23**, 3457–3473, doi: 10.1175/2009JCLI3136.1.

Yuan, T. L., J. V. Martins, Z. Q. Li, and L. A. Remer, 2010: Estimating glaciation temperature of deep convective clouds with remote sensing data. *Geophys. Res. Lett.*, **37**, L08808, doi: 10.1029/2010GL042753.

Zhang, H., J. Peng, X. W. Jing, and J. N. Li, 2013: The features of cloud overlapping in Eastern Asia and their effect on cloud radiative forcing. *Sci. China* (*Earth*), **56**, 737–747, doi: 10.1007/s11430-012-4489-x.